Computers and Fluids 251 (2023) 105760

Contents lists available at ScienceDirect

Computers and Fluids

journal homepage: www.elsevier.com/locate/compfluid

Characteristic spanwise length scales of streamwise vortical structures in the wake of a circular cylinder at $Re = 1500$ measured via global and local approaches

Wasim Sarwar [a], Reda El Mansy [b], Josep M. Bergadà [b], Fernando Mellibovsky [a,*]

[a] Department of Physics, Aerospace Engineering Division, Universitat Politècnica de Catalunya, 08034, Barcelona, Spain
[b] Department of Fluid Mechanics, Universitat Politècnica de Catalunya, 08034, Barcelona, Spain

ARTICLE INFO

Keywords:
Direct numerical simulation
Incompressible flow
Cylinder wake instability
Hilberttransform
Autocorrelation
Aerodynamic forces

ABSTRACT

Wake characteristics of the flow past a circular cylinder are analysed in detail at Reynolds number $Re = 1500$ via direct numerical simulation. A periodic spanwise domain of length $1.5\pi D$ has been found to yield correct first- and second-order wake statistics in remarkable agreement with published results at the same and closeby Re. A Kelvin–Helmholtz instability with a frequency $f_{\mathrm{KH}} \simeq 0.666$ is observed to occur intermittently in the shear layers issued from the top and bottom of the cylinder. The three-dimensional patterns in the wake have an estimated spanwise length scale $l_z^1/D \simeq 0.70$ (D is the cylinder diameter) in the near-wake at $(x, y)/D = (3, 0.5)$, downstream from the cylinder, when quantified by autocorrelation (global approach). When using the Hilbert-transform (local approach) instead, the predicted length scale of streamwise vortical structures is distributed around $\lambda_z/D \simeq 0.33$ at the same sampling location. Our results show that the two approaches measure different aspects of three-dimensionality: while the former informs of the typical spanwise spacing of streamwise vortices, the latter quantifies the local spanwise size of these same flow structures.

1. Introduction

There has been a spurt of research activity regarding bluff body wakes over the past few decades which is in part triggered by the fundamental importance of wake flows [1], and in part by the plethora of practical industrial applications [2,3]. Because of its tempting simplicity, the flow past circular cylinders has been employed as the canonic geometric arrangement in both experimental and numerical setups, and a wealth of knowledge has been accumulated by scientists and engineers alike over the years using cutting-edge experimental techniques such as particle image velocimetry (PIV) [4,5] or laser Doppler anemometry [6], and state-of-the-art numerical methods allowing direct numerical simulation (DNS) in first-rate supercomputing facilities [7,8]. The flow past a circular cylinder is considered a paradigm for bluff body aerodynamics, and a profusion of detailed experimental, numerical and analytic studies exist that are devoted to the analysis and understanding of boundary layer separation, shear layer interactions, wake vortex formation, inception and development of three-dimensional vortical structures, and wake turbulent transition.

At sufficiently low values of the Reynolds number ($Re \equiv UD/\nu$, based on cylinder diameter D, upstream flow velocity U and fluid kinematic viscosity ν), the flow past a circular cylinder placed in a homogeneous crossflow features a time-independent state characterised by two symmetric recirculating regions attached to the rear of the cylinder. This steady solution destabilises into a two-dimensional space–time-symmetric solution in a supercritical Hopf bifurcation, which manifests itself in the form of the well-known von-Kármán vortex street. The characteristic alternate shedding of vortical structures from the opposite sides of the cylinder results in an unsteady aerodynamic force with components in both the axial and crossflow direction which is the source of vibration [1] and noise [9], which may entail structure failure or be exploited in energy harvesting applications [10,11].

The two-dimensional space–time-symmetric periodic state is overruled by the onset of three-dimensionality for $Re \gtrsim 190$, spanwise dependence being characterised by the inception of hysteretic mode A first, followed suit by the emergence of mode B in the so-called wake transition regime $Re \in [190, 260]$. The appearance of these instability modes has been linked to the observation of discontinuities of the Strouhal number when smoothly varying Re [12]. Mode A is subcritical and is related to the onset of vortex loops and the subsequent formation of streamwise vortex pairs in the cylinder wake with characteristic wavelength $\lambda_z^{\mathrm{A}}/D \simeq 3 \sim 4$ at $Re \gtrsim 180$, while mode B, featuring smaller-scale streamwise vortex pairs of wavelength $\lambda_z^{\mathrm{B}}/D \sim 1$, is observed over

* Corresponding author.
E-mail address: fernando.mellibovsky@upc.edu (F. Mellibovsky).

https://doi.org/10.1016/j.compfluid.2022.105760
Received 23 June 2022; Received in revised form 4 November 2022; Accepted 8 December 2022
Available online 13 December 2022

a range of $Re \in [230-250]$, the evolution from the former mode to the latter being characterised by a gradual energy transfer [12]. In addition to the aforementioned three-dimensional modes, there exist local phase dislocations that generate large-scale-spot-like structures [13,14] that propagate downstream of the cylinder base and render the mode A regime spatio-temporally irregular.

The shear layers separated from the opposite sides of the cylinder may be subject to laminar–turbulent transition at sufficiently high Re [14]. This transition is initiated by the onset of a spatially-developing Kelvin–Helmholtz instability that results in a growing train of vortices of relatively small length and time scale. The critical Reynolds number for the onset of the shear layer instability has been reported widely spread over a large range of Re [14–17], allegedly bearing a strong dependence on the background disturbance, experimental conditions, cylinder ends, etc. The ratio of shear-layer to von-Kármán frequency has been observed to scale with Re with an exponent that also presents some scatter among different sources [14,17–19].

A number of research studies have evaluated the spanwise length scale of three-dimensional wake instabilities using both flow visualisation and mathematical/numerical techniques such as autocorrelation [20], Hilbert-transform [7], wavelet-transform [21], and several others. These various methods have produced reasonably accurate and consistent measurements for λ_z^A and λ_z^B in the so-called wake-transition regime. Beyond this point, the variation of the spanwise length scales of longitudinal vortices have been experimentally reported to scale inversely with Re as $1/\sqrt{Re}$ in the range $Re \in [300-2200]$ [20] using two-probe correlation. A discrepancy of spanwise structures size was however observed between the experimental scaling law [20] and numerical results [22] at coincident Re, which might be ascribed to the application of different definitions and/or measuring techniques. Also the dependence of spanwise vortex size on measuring streamwise and cross-stream location along the cylinder wake has been shown to disagree among a number of experimental [20,23] and numerical [7,22] studies. The near-wake crossflow sampling location appears to have a significant impact on the results, while the far-wake is less sensitive to sampling location and produces a more stable typical spanwise size of the structures.

In this work, we investigate the flow past a circular cylinder at $Re = 1500$, with the shear layer instability in its early stages of development and therefore barely perceptible, and laminarity preserved over a fair portion of the shear layer. The spanwise length scales of the streamwise vortices that arise following the secondary three-dimensionalising instability of the cylinder wake will be characterised in detail using both global (two-probe cross-correlation) and local (Hilbert transform) approaches. Even-though both approaches have been applied in the characterisation of the secondary instability in the past at higher Re, this is the first time, to the authors knowledge, that both techniques are used concurrently on the same dataset to allow comparison and understand the differences. We shall not be concerned here with the large-scale dislocations that appear across the wake transition regime, but with the shorter-scale streamwise vortices that form the regular pattern that eventually dislocates.

The outline of the paper is as follows. The mathematical formulation is presented in section Section 2 alongside the numerical approach undertaken to solve the equations of motion. Section Section 3 reports the numerical results in terms of global quantities first, followed by near-wake first- and second-order statistics along the wake-centreline, and concludes with a characterisation of the shear layers instability as they synchronously flap in the near-wake. Section 4 is devoted to the characterisation of the three-dimensionalising secondary wake instability and analyses the resulting turbulent-wake spanwise structures using both autocorrelation and Hilbert-transform. Finally, the main findings are summarised in Section 5.

2. Problem formulation and numerical approach

We consider the incompressible viscous flow of a Newtonian fluid of kinematic viscosity ν past a cylinder of circular cross-section. The dynamics is governed by the Navier–Stokes equations, which after non-dimensionalisation with the cylinder diameter D, and the incoming flow velocity U yields

$$\begin{aligned} \frac{\partial \mathbf{u}}{\partial t} + (\mathbf{u}\cdot\nabla)\mathbf{u} &= -\nabla p + \frac{1}{Re}\nabla^2\mathbf{u}, \\ \nabla\cdot\mathbf{u} &= 0, \end{aligned} \tag{1}$$

where $\mathbf{u}(\mathbf{x};t) = (u,v,w)$ and $p(\mathbf{x};t)$ are the velocity and pressure, respectively, at the nondimensional location $\mathbf{x} = (x,y,z)$ and convective time t. The cartesian nondimensional coordinates x, y and z indicate location in the streamwise, crossflow and spanwise directions and u, v and w are the corresponding velocity components. The sole governing parameter, $Re = UD/\nu$, is the Reynolds number. Units will be omitted from this point on, as they are implied by the non-dimensionalisation length and velocity scales. A computational domain of size $[-20,50]\times[-20,20]\times[0,1.5\pi]$ in the streamwise, cross-stream and spanwise directions has been used for the numerical simulation (Fig. 1).

A unitary velocity $\mathbf{u}(-20,y,z;t) = (1,0,0)$ is prescribed at the inlet, the cylinder walls are no-slip, and the top and bottom boundaries set as slip walls. In all three boundaries, Neumann pressure boundary conditions are used, while a homogeneous Dirichlet pressure boundary condition is prescribed at outlet. A periodic boundary condition is enforced in the spanwise direction for all fields.

The direct numerical simulation (DNS) has been performed with an incompressible Navier–Stokes solver provided by the open source software OpenFOAM [24], which is based on a finite volume formulation. The time integration has been done with a second-order-accurate Crank-Nicholson central-difference scheme and a time step $\Delta t = 0.0005$. The space discretisation is based on second-order upwind and central-differences for the advection and diffusion terms, respectively. The pressure–velocity coupling is tackled with the Pressure-Implicit with Splitting of the Operators (PISO) [25] scheme, using the Preconditioned Conjugate Gradient (PCG) solver for the pressure equation, and the Preconditioned Bi-Conjugate Gradient (PBiCG) for all three velocity equations.

3. Numerical validation against benchmark data

Table 1 compares the present simulation with previous experimental and numerical studies at the same and neighbouring values of the Reynolds number. The in-plane cell count has been set high to 201×10^3 in order to compensate for the low order of the finite-volumes spatial discretisation. The number of in-plane degrees of freedom considered is comparable to that used by Sarwar and Mellibovsky [22], somewhat larger at $548\times8^2 \simeq 351\times10^3$ but considering a slightly higher flow regime $Re = 2000$, and way larger than all other numerical studies reported [4,7,8,26–28]. A lower bound for the Kolmogorov length scale in the near wake has been estimated, from the average dissipation rate of turbulent kinetic energy and assuming isotropic turbulence, at about $\eta \simeq 0.02$, which is commensurate with the typical cell size deployed in the region. The power spectrum of the streamwise velocity signal at several streamwise off-centreline locations with $y = 0.5$ along the wake, shown in Fig. 2a, provides yet additional confirmation that the mesh and method are adequate to capture the whole extent of the inertial subrange and reach deep into the dissipation scales. Besides the conspicuous peaks at the vortex shedding frequency and harmonics, the spectra clearly conform to the $-5/3$ energy decay rate that is typical of the inertial subrange (see straight line) before viscous dissipation kicks in at higher frequency.

The spanwise extent of the domain is fairly large at $L_z = 1.5\pi$, sufficient to accommodate up to 9 streamwise vortex pairs of a typical wavelength $\lambda_z \simeq 0.52D$ at $(x,y) = (3,0.5)$ and $Re = 1500$, according to the experimental scaling law by Mansy et al. [20], who defined

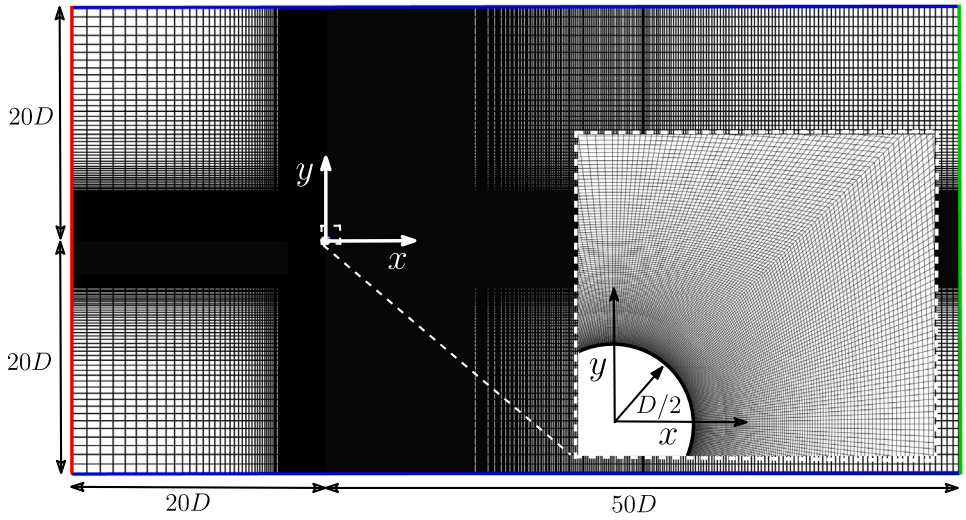

Fig. 1. Sketch of the computational domain and mesh. The streamwise-crossflow (x, y)-plane is discretised with a high-density mesh in the critical areas. The inset shows a detail of the mesh around the cylinder.

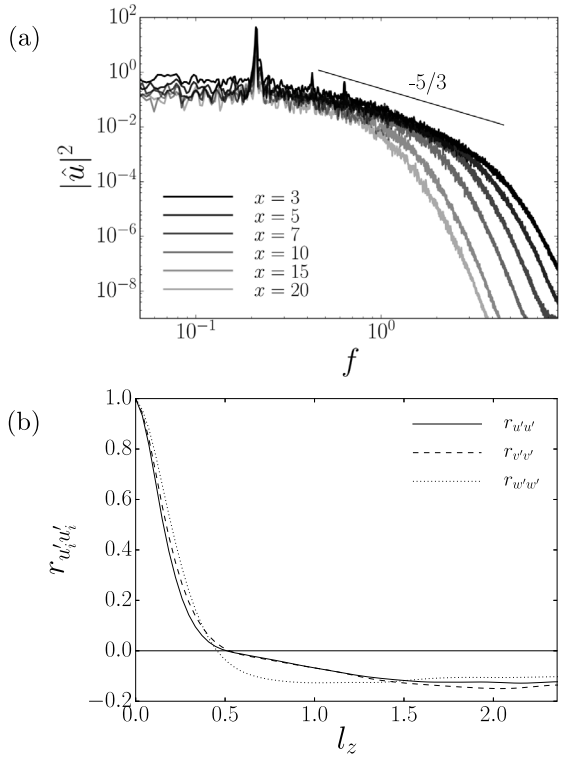

Fig. 2. (a) Spanwise-averaged spectrum $|\hat{u}|^2$ of the streamwise velocity signal $u(x, 0.5, z; t)$ at several off-centreline streamwise locations. The straight line indicates the $-5/3$ slope typical of the inertial subrange. (b) Spanwise autocorrelations of fluctuation velocity components $r_{u'u'}$, $r_{v'v'}$ and $r_{w'w'}$ at off-centerline location $(x, y) = (3, 0.5)$ for $Re = 1500$.

the characteristic length scale using the first peak of the normalised instantaneous spanwise autocorrelation of streamwise velocity. The spanwise wavelength was shown to increase progressively downstream before reaching saturation at about $\lambda_z \simeq 1.0D$ beyond $x \geq 10$ for $Re \in [1100, 2000]$, such that 4 to 5 vortex pairs would still fit in our domain. In order to further assess the sufficiency of the spanwise extent of the domain, one might use time-averaged normalised spanwise autocorrelation of velocity fluctuations

$$r_{u_i'u_i'}(l_z; x, y) = \frac{\langle u_i'(x, y, z; t) u_i'(x, y, z - l_z; t) \rangle_{z,t}}{\langle u_i'(x, y, z; t)^2 \rangle_{z,t}}, \tag{2}$$

where $u_i'(x, y, z; t) = \langle u_i(x, y, z; t) \rangle_{z,t} - u_i(x, y, z; t)$ and the subindex in $u_i = \{u, v, w\}$ denotes each of the three cartesian components of velocity. Fig. 2b shows these autocorrelations for $Re = 1500$ at the off-centreline location $(x, y) = (3, 0.5)$. All three velocity components decorrelate fast initially, but saturation follows shortly, such that autocorrelation values stagnate at about $r_{u_i'u_i'}(l_z; 3, 0.5) \simeq -0.1$. Similar values are obtained at the several off-centreline locations we have tested along the wake for $y = 0.5$ and $x \in [2, 20]$ (not shown). These results are in line with the observations of Wissink and Rodi [29] using streamwise velocity at several streamwise locations $x \in [2, 8]$ along the wake centreline $y = 0$ for $Re = 3300$ in a domain with $L_z = 8$, which led them to conclude that the spanwise extent might not be sufficient. Comparable decorrelation levels at off-centreline locations were instead considered sufficient by Ramberg and Griffin [30] for $L_z = 10$ at $Re \in [500, 600]$ and by Evangelinos [31] for $L_z = 6$ at $Re = 1000$. According to the decreasing trend, our $L_z = 1.5\pi$ would be suitable at $Re = 1500$. The residual autocorrelation could certainly hint at the possible existence of large-scale spanwise flow structures, but the decorrelation is still substantial enough to assume that long wavelength modulation, if allowed for by employing sufficiently large domains, would be fairly low amplitude and not significantly affect the properties of the vortical structures of interest here.

Using $N_z = 128$ spanwise grid planes yields a spanwise resolution density $N_z/L_z \simeq 27.1$, which is not overly high but deemed sufficient to properly capture the smallest spanwise features of the flow. Statistics are collected over 125 vortex-shedding cycles so that convergence can be safely claimed. This should in principle allow detection of the low-frequency wake fluctuation reported by Lehmkuhl et al. [34] at $Re = 3900$, and we have indeed found some evidence that this might also be occurring at $Re = 1500$. Increasing the in-plane resolution to 241×10^3 cells, and the spanwise resolution and size of the domain to 256 and 2π, respectively, produced no significant changes in the results despite the much shorter data sample achievable in a reasonable time-span.

Since the Strouhal number (von Kármán vortex-shedding frequency) is known to present an almost flat trend across the flow regime under scrutiny [35], it can be expected that our numerically computed frequency $f_{\text{vK}} = 0.212$ at $Re = 1500$ should agree well with published results at neighbouring values of Re. As it happens, the agreement is fair with all reported experimental [5,19,32,33] and numerical [19,32,36,37] values for $Re \in [1500, 3900]$. Similarly, mean drag values are consistent with both experimental [19] and numerical [22,26] results at close-by Re if allowance is made for the slightly increasing trend that is to be expected. The recirculation bubble length L_r is instead known

Table 1
Experimental and numerical literature survey of circular cylinder in crossflow. Listed in the table are the spanwise domain length L_z, spanwise N_z and in-plane N_{xy} grid resolutions (discretisation order in superscript, ^{F} for Fourier), free stream turbulence intensity Tu, number of vortex-shedding cycles used in computing statistics N_s, vortex-shedding frequency f_{vK}, shear-layer frequency f_{KH}, recirculation bubble length L_r, boundary layer separation point θ_{sep}, and shape of the cross-stream profile of mean streamwise velocity in the near-wake at $x/D = 3$ behind cylinder.

Numerical													
Author [Ref]	Method	Re	L_z	N_z	N_{xy}	N_s	f_{vK}	f_{KH}	L_r	C_D	$-C_{p_b}$	θ_{sep}	Sol.
Present results:	DNS FVM	1500	1.5π	128	241×10^3	125	0.212	0.666	1.72	0.969	0.78	90.0	U
Sarwar and Mellibovsky [22]	DNS SEM	2000	2.5	128^F	5484^8	55	0.215	0.839	1.66	0.975	0.80	90.0	U
	DNS SEM	2000	π	96^F	5484^8	22	0.211		1.71	0.961	0.79	90.0	U
Gsell et al. [7]	DNS FVM	3900	10	300	150×10^3	3–4	0.210	1.365		0.92		86.8	
Ma et al. [8]	DNS SEM	3900	π	128^F	902^{10}		0.219		1.59		0.84		U
			1.5π	64^F	902^{10}		0.206		1.00		1.04		V
			2π	256^F	902^8		0.203		1.12		0.96		V
($c_s = 0.032$)	LES SEM		1.5π	64^F	902^8		0.213		1.28		0.90		UV
($c_s = 0.196$)			1.5π	64^F	902^8		0.208		1.76		0.77		U
Dong et al. [4]	DNS SEM	3900	π	128^F	902^8	40–50	0.210	1.539	1.36				UV
			1.5π	192^F	902^8		0.208		1.18		0.93		V
				128^F			0.210		1.12		0.96		V
				64^F			0.206		1.00		1.04		V
Chen et al. [26]	iLES FVM	2580	π	56	70×10^3	50	0.220		1.66	0.95	0.73		U
				20	12.5×10^3	50	0.220		1.13	1.03	0.88		V
Mohammad et al. [28]	iLES SDM	2580	π	18^3	$11\,144^3$	20							U
				18^2	7880^2	20							V
				12^3	7880^3	20							U
Lodato and Jameson [27]	iLES SDM	2580	3.2	10^3	1847^3	300							U

Experimental										
Author [Ref]	Method	Re	L_z	Tu	N_s	f_{vK}		L_r	C_D	$-C_{p_b}$
Norberg [19]	HWA	2000	240	~0.1%		0.213				
		3000	80	~0.1%		0.213		1.65	0.98	0.84
		3000	80	~1.4%		0.209		1.44	1.03	0.89
Norberg [6]	LDV	1500	65	<0.1%	1350		1.75	1.79		
		3000	65	<0.1%				1.66		
Norberg [32]	LDV	1500	105	<0.1%		0.212				
Konstantinidis et al. [33]	LDV	1550	10	~3.3%						
		2150	10	~3.3%		0.215		1.77		
		2750	10	~3.3%						
Konstantinidis and Balabani [5]	PIV	2150	10	~3.3%		0.215		1.58		

to notably decrease across the shear layer instability regime [38]. This explains why the value obtained, $L_r = 1.72$, is similar to that found in experiments [6,33] and well-resolved numerical simulations [22,26] for $Re < 2600$ but considerably higher than reported values for $Re > 3000$ [4,8,19].

Fig. 3a depicts the mean pressure coefficient ($C_p(\theta)$, grey solid line) distribution along the cylinder wall from the front stagnation point at $\theta = 0°$ to the cylinder base point at $\theta = 180°$. Agreement with experiments by Norberg [35] at the same $Re = 1500$ is excellent. Pressure is maximum at the stagnation point and decreases fast as the flow accelerates along the front portion of the cylinder. A minimum is reached somewhat ahead of the highest point on the surface and starts recovering. The recovery is nevertheless not complete, as separation is observed to occur at $\theta \simeq 90.0°$ (see zero crossing of the C_f distribution, grey dashed line). The C_p stabilises thereafter at a fairly constant negative value (suction) that is maintained all the way down to the base point.

The average streamlines issued symmetrically from the separation points at either side of the cylinder coalesce in a statistically quiescent flow some distance behind the cylinder, whence two purely streamwise streamlines emanate, one pointing upstream towards the base point and the other extending downstream to infinity. The streamlines arrangement conforms a two-lobed-symmetric recirculated flow region, attached to the cylinder back surface, where fluid is trapped on average. The quiescent flow point bounding it at the rear is used in defining a recirculation bubble length L_r, which is known to inversely correlate with base pressure and, therefore, the drag coefficient [39]. Along the two streamlines issued from the separation points extend the shear layers resulting from the separated boundary layers. The cross-stream gradients of streamwise velocity are large across the shear layers and contribute in triggering the Kelvin–Helmholtz instability that is intermittently detected.

Fig. 3b (top) shows the mean streamwise velocity distribution $\bar{u}(x, 0)$ along the wake centreline of the present numerical solution along with experimental measurements at the same and close-by values of Re. The mean streamwise velocity $\bar{u}$ is negative in the close vicinity of the cylinder base, as the fluid recirculates there, and the distance to the zero-crossing provides the definition for the recirculation bubble length $L_r = 1.72$. Downstream from the quiescent flow point, $\bar{u}$ recovers fast in the near wake but the recovery rate soon slows down and saturates at an imperceptible slope in the mid wake. The streamwise velocity in the wake centreline remains defective, with respect to free-stream velocity, for a very long distance behind the cylinder. The upstream shift of both $\bar{u}(x, 0)_{min}$ and the zero-crossing evinces that the recirculation bubble shrinks as Re is increased. The agreement with experimental results at the same [6] and similar [33] Re is good as regards the trends and the location of the lowest mean velocity and zero crossing, but $\bar{u}(x, 0)_{min}$ appears to be somewhat underestimated in our computations as compared to Norberg [6]. This same discrepancy with respect to Norberg [6] is systematically observed in all other well-resolved numerical studies that analysed the mean streamwise velocity distribution along the wake centreline at closeby Re (see e.g. [34,37]). We believe that the mismatch is related to a shortcoming in the experimental measurements, given that the agreement is instead fair when comparing with Konstantinidis et al. [33].

The wake centreline distribution of streamwise velocity covariance ($\langle u'u' \rangle$ in Fig. 3b-bottom) shows the characteristic two-peak distribution typically reported in experiments [6,33,37]. While the first peak follows from vortex formation, the second peak has been ascribed to the cross-over of mode-B-type longitudinal vortices [6]. The shape and streamwise location of the peaks comply with experimental measurements at the same Re [6], but their magnitude is severely under-predicted. At the slightly higher $Re = 2000$ [22] numerics seem

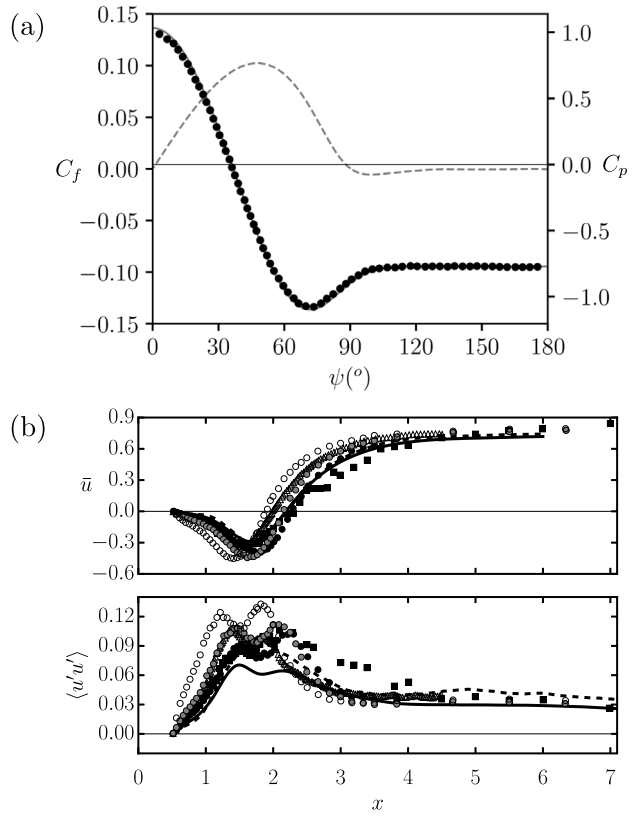

Fig. 3. (a) Mean pressure (C_p, solid grey) and friction (C_f, dashed grey) coefficient distribution along the cylinder wall at $Re = 1500$ (solid line). Circles indicate experimental measurements by Norberg [35]. (b) Streamwise velocity first- (top, mean $\bar{u}$) and second-order (bottom, covariance $\langle u'u' \rangle$) near-wake statistics distribution along the wake centreline. Shown are the present results (solid line, $Re = 1500$), numerical results by Sarwar and Mellibovsky [22] (dashed line, $Re = 2000$), and experiments also by Norberg [6] (circles: black, $Re = 1500$; grey, $Re = 3000$; white, $Re = 5000$), Konstantinidis et al. [33] (black squares, $Re = 2150$) and Parnaudeau et al. [37] (white triangles, $Re = 3900$).

to closely match the experiments of Norberg [6] at $Re = 1500$, while one would expect the peak to fall half way between experimental values at $Re = 1500$ and 3000. Whereas the trend with Re seems right, numerical results fall consistently short of experimental measurements. As was the case with mean streamwise velocity distribution along the wake centreline, the experiments by Norberg [6] report streamwise normal Reynolds stress distributions systematically higher than found elsewhere [34,37]. Again, some flaws in the experimental determination of instantaneous velocity in this rather active region of the wake might be held responsible. The dissimilar inflection point and peak $\langle u'u' \rangle(x, 0)$ distribution reported by Konstantinidis et al. [33] at $Re = 2150$ is most probably the result of high free-stream turbulence ($Tu \sim 3.3\%$) advancing the turbulent transition along the detached shear layers. As for the mean velocity, the covariance peaks also shift upstream towards the cylinder as Re is increased. The vortex formation region length (L_f) is accordingly shortened, which also contributes to the drag coefficient increase.

Near-wake dynamics might be analysed comprehensively through the inspection of time signals obtained from spanwise probe arrays conveniently embedded in the detached shear layer. Vortex-shedding dynamics might be captured with probes located anywhere in the wake, but to allow detection of an incipient Kelvin–Helmholtz instability, the probe location must be chosen along the time-averaged shear layer, upstream from the vortex formation region to avoid excessive flapping, but far downstream from the separation point for an eventual

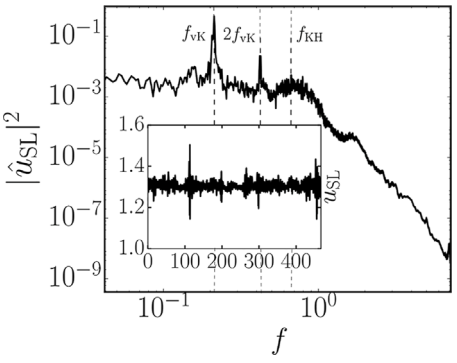

Fig. 4. Spanwise-averaged power spectrum $|\hat{u}_{SL}|^2$ of the streamwise velocity signals $u_{SL}(z;t) = u(1, 0.8, z; t)$ along a spanwise probe array submerged in the shear layer. The inset shows one such signal at an arbitrary z location.

instability to have had space to develop sufficiently. The inset of Fig. 4 shows the instantaneous streamwise velocity signal of a point probe $u_{SL}(t) = u(1, 0.8, z; t)$ at some arbitrary spanwise location z. The low-amplitude low-frequency fluctuations are related to shear layer flapping due to the formation of Kármán vortices in the wake. The occasional high-amplitude peaks have a higher frequency associated, that can be traced to a shear layer instability that is not sustained permanently. The spanwise-averaged streamwise velocity spectrum $|\hat{u}_{SL}|$ in Fig. 4 helps identify the underlying frequencies of the wake. The clear sharp peak at $f_{vK} = 0.212$ and its harmonic $2f_{vK}$ are the result of a regular vortex-shedding process in the wake. A broadband energy spread around $f_{KH} = 0.666$, resulting from the intermittent high-amplitude high-frequency fluctuation bursts, might be ascribed to an inherent Kelvin–Helmholtz instability of the shear layer. This value is in remarkably good agreement with experimental measurements by Prasad and Williamson [17], which displayed a similar space–time dependence that was already acknowledged by Sarwar and Mellibovsky [22].

A close look into the shear layers provides some insight into the origin and nature of velocity fluctuations. Fig. 5 depicts colour maps of fluctuation kinetic energy and normal Reynolds stress fields in the near-wake region. The contour levels are evenly distributed in logarithmic scale so as to expose any linear mechanism that may govern the amplification of fluctuations within the shear layer. Fluctuation kinetic energy $k = (\langle u'u' \rangle + \langle v'v' \rangle + \langle w'w' \rangle)/2$ (Fig. 5a) increases fast along the narrow strip that delimits the average shear layer (see red dashed line) whence it diffuses into the recirculation region of the wake. The growth is essentially led by the normal streamwise component $\langle u'u' \rangle$ of the Reynolds stress tensor (Fig. 5b), with the spanwise component $\langle w'w' \rangle$ (Fig. 5d) trailing behind. The cross-stream component $\langle v'v' \rangle$ (Fig. 5c) remains instead very low over a long portion of the shear layer, while turbulent mixing amplifies it considerably within the recirculation bubble to values comparable to the other two components. The evolution of all four quantities along the mean shear layer centreline (red dashed line), defined as the loci of points with the highest mean transverse shear, are shown in Fig. 6. The fluctuation kinetic energy k grows subexponentially along the shear layer and is clearly dominated by the streamwise normal Reynolds stress $\langle u'u' \rangle$. The cross-stream component $\langle v'v' \rangle$, which together with $\langle u'u' \rangle$ inevitably contains the fluctuations induced by two-dimensional vortex shedding, starts over one order of magnitude below at the root of the shear layer and, despite growing exponentially, remains always smaller in magnitude. The spanwise component $\langle w'w' \rangle$, which is instead purely a product of three-dimensionalisation, starts as low as $\langle v'v' \rangle$, but grows exponentially at a much faster rate before saturation occurs. It is unclear whether the exponential growths of $\langle v'v' \rangle$ or $\langle w'w' \rangle$ could follow from a linear instability of the mean shear layer, particularly so when the fastest growing component cannot be interpreted in the light of a Kelvin–Helmholtz instability, which would be two-dimensional in nature.

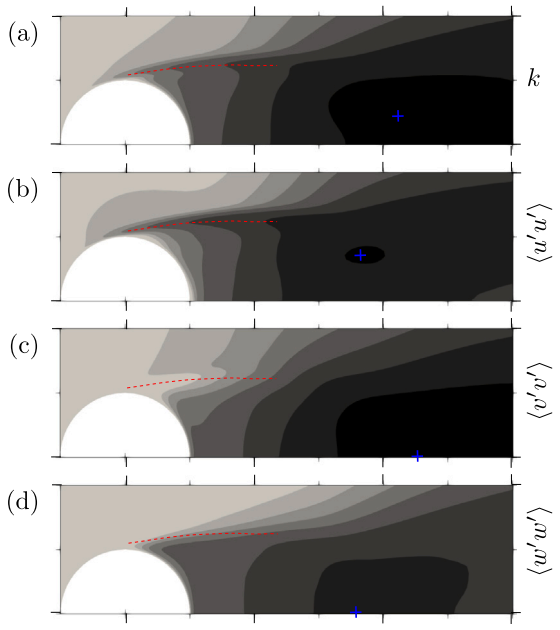

Fig. 5. Shear layer and near wake velocity fluctuation statistics. (a) Fluctuation kinetic energy $k = (\langle u'u' \rangle + \langle v'v' \rangle + \langle w'w' \rangle)/2$. (b) Streamwise $\langle u'u' \rangle$, (c) cross-stream $\langle v'v' \rangle$ and (d) spanwise $\langle w'w' \rangle$ normal Reynolds stress components. Eight colour levels have been evenly distributed in the logarithmic range $[5 \times 10^{-5}, 0.5]$ in factors of $\sqrt{10}$. The red dashed line indicates the core of the shear layer. The peak location for each field is marked with a blue plus sign.

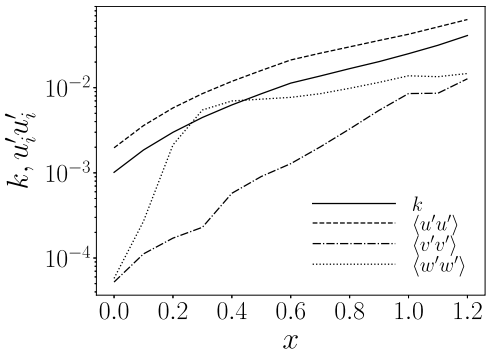

Fig. 6. Normal Reynolds stresses ($\langle u'u' \rangle$, $\langle v'v' \rangle$, $\langle w'w' \rangle$) and fluctuation kinetic energy (k) evolution along the shear layer (see red dashed line of Fig. 5).

4. Results and discussion

Flow visualisation has been routinely used in experimental studies to estimate the typical spanwise size of large-scale three-dimensional coherent structures in the cylinder wake [40]. A more systematic analysis might however be carried out employing mathematically rigorous methods such as autocorrelation [20], Fourier, Hilbert–Huang [7] or wavelet transforms, spectrogram, etc. Each one of these methods, when applied to a spanwise dependent signal, is capable of capturing different three-dimensional aspects of the flow patterns present in the cylinder wake. Autocorrelation and Fourier transform are usually favoured due to their simplicity, and constitute an ideal choice whenever the three-dimensional flow structures are regularly distributed along the span. Both methods act globally, and as such are better suited for flow structures that result from global pattern-forming instabilities and pervade the full span of the wake. The Hilbert, Huang–Hilbert and wavelet transforms capture instead local features of the signal, and are therefore more appropriate in detecting and characterising structures that exhibit localisation in the spanwise coordinate. It is

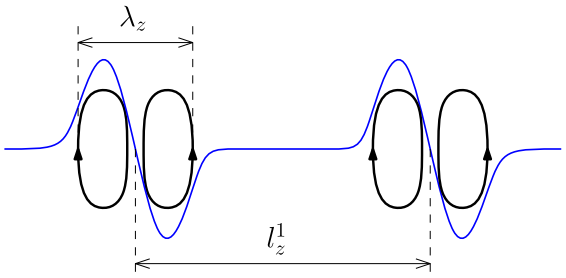

Fig. 7. Sketch of the two different spanwise length scales that are targeted by global (vortex spacing l_z^1) and local (vortex size λ_z) approaches, respectively. The blue line represents the spanwise dependence of some perturbation signal under scrutiny.

therefore to be expected that while global methods provide a measurement of the typical spanwise spacing of three-dimensional vortical structures, local methods yield estimates for their characteristic spanwise size instead. The sketch of Fig. 7 represents schematically the difference between the two length scales. They necessarily coincide at the three-dimensionalising instability, where the bifurcated solution is just a modal perturbation of the underlying two-dimensional flow (the perturbation field is perfectly sinusoidal in the spanwise direction at the critical Reynolds number), but as the solution develops nonlinearly, vortices tend to concentrate and perhaps even localise while their spacing (related to the number per unit span that can be packed comfortably together) may evolve otherwise. In experiments or time-stepping numerical simulations, the two length scales may be different from outset whenever the three-dimensionalising bifurcation is subcritical, as is the case of mode A for the circular cylinder.

In the cylinder wake at $Re = 1500$, three-dimensional vortical structures are typically organised in a pseudo-periodic spanwise array, but the irregularity of the pattern is sufficient to claim that local effects are also at play. Isolated vortical structures seldom occur, as is also the case at higher $Re = 2000$ [22], but the spacing between concurrent streamwise vortices is often large enough for them to decorrelate to some extent. Here we employ autocorrelation and the Hilbert transform, as representing global and local approaches, respectively, to independently analyse the typical spanwise spacing and characteristic spanwise size of streamwise vortices appearing in the cylinder wake in the transitional regime at $Re = 1500$, in an attempt to clarify to what degree these two length scales have become independent from one another.

The signal we use to analyse the presence of streamwise-cross-stream vortical structures in the wake is the spanwise gradient of streamwise velocity $\tilde{\omega}_y(z;t) \equiv \partial_z u(3, 0.5, z; t)$, which provides an indirect measurement of cross-stream vorticity. The sampling location lies just downstream of the recirculation region, where three-dimensionality is dominant between the braids connecting consecutive Kármán vortices, and at a cross-stream height conveniently aligned with the mean shear layer issued from the top of the cylinder, such that the passage of top Kármán vortices can be readily detected [20,22]. Following Sarwar and Mellibovsky [22], the local spanwise size of the vortical structures is accordingly measured by computing the corresponding analytic signal

$$\tilde{\omega}_y^a = \tilde{\omega}_y + \mathrm{i}\mathcal{H}(\tilde{\omega}_y) = A_\omega \mathrm{e}^{\mathrm{i}\varphi_\omega} \tag{3}$$

where $\mathcal{H}$ denotes the Hilbert transform, and $A_\omega(z;t)$ and $\varphi_\omega(z;t) \equiv \arg(\tilde{\omega}_y^a)$ are the amplitude and phase, respectively. The latter provides a definition for the local spanwise size of the vortical structures following

$$\frac{2\pi}{\lambda_z(z,t)} = \frac{d\varphi_\omega}{dz}, \tag{4}$$

while the former informs of its local intensity.

The probability density function (PDF) of λ_z is assessed via normal/Gaussian kernel density estimation (KDE) with bandwidth $w =$

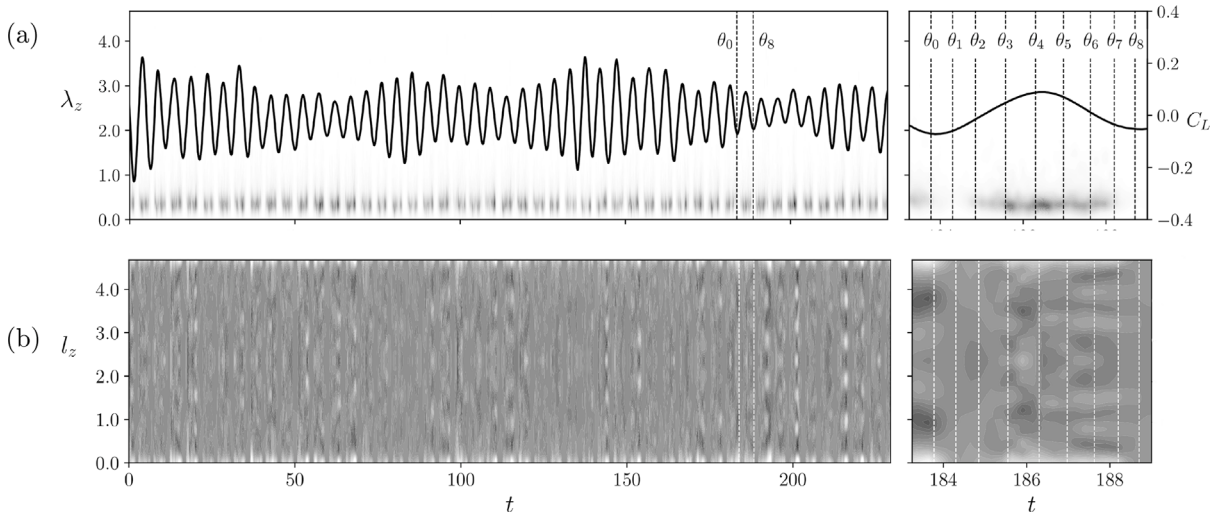

Fig. 8. Time evolution of (a) the probability density function of the local spanwise size PDF(λ_z, t) duly weighed by instantaneous local amplitude A_ω, and (b) the autocorrelation function $R_{u'u'}(l_z, t)$. The C_L signal used in defining an instantaneous phase has been superimposed to panel (a). The panels to the right correspond to details and 8 equispaced instantaneous phases along a vortex-shedding cycle are indicated with vertical dashed lines and labelled $\theta_i = i\pi/2$, $i \in \{0, 1, 2, 3, \dots 7\}$.

0.02, and used to identify the typical spanwise size λ_z of vortical structures along the probe-array. Fig. 8a represents the time evolution of A_ω-weighed contours of PDF($\lambda_z(z, t)$). The dark regions denote the presence of strong three-dimensional spanwise structures of the corresponding typical size, while white indicates absence of streamwise-cross-stream vortical activity. The synchronous recurrent pattern of dark spots reveals that three-dimensionality chiefly occurs at certain phases of the vortex-shedding process, and that, when present, spanwise vortical structures have a preferred characteristic size that is rather small at $\lambda_z \simeq 0.33$. Also drawn in Fig. 8a is the C_L signal, which provides timely information on the vortex-shedding cycle. The C_L time series can also be used in defining an instantaneous phase. This has been done by using again the Hilbert transform to produce an analytic signal $C_L^a = C_L + \mathrm{i}\mathcal{H}(C_L)$ whose phase is readily obtained as $\theta \equiv \arg(C_L^a)$.

The panel to the right shows a detail covering just over a full vortex-shedding cycle. Eight equispaced phases have been indicated with vertical dashed lines and labelled $\theta_i = i\pi/4$, $i \in \{0, 1, 2, \dots, 7\}$. Note that these equispaced phases, univocally defined via de Hilbert transform of the C_L signal, may not correspond to equal time intervals, as the phase and time parametrisations may locally stretch or shrink with respect to each other along any particular vortex shedding cycle. At θ_0, the probe-array does not register any indication of three-dimensionality, which gradually builds up through θ_1 and θ_2 and peaks at θ_3. Afterwards streamwise-cross-stream vortical structures fade fast and are rather weak in the interval between θ_4 and θ_5, whence three-dimensionality reactivates anew and reaches a second peak, higher than the previous one, at about θ_6. Past this peak, spanwise structure decays altogether and the flow becomes predominantly two-dimensional beyond θ_7 and $\theta_8 = \theta_0$.

The spanwise modulation component of the streamwise velocity signal $u'(z, t) \equiv u(z, t) - \langle u(z, t)\rangle_z$ has been used to detect spanwise patterns via non-normalised autocorrelation, which is defined and estimated as

$$R_{u'u'}(l_z, t) = \frac{1}{L_z}\int_0^{L_z} u'(z, t)u'(z - l_z, t)\, dz \simeq \simeq \frac{1}{N}\sum_{i=0}^{N-1} u'(z_i, t)u'(z_i - l_z, t). \tag{5}$$

Here, the L_z periodicity is duly exploited and the discrete autocorrelation function evaluated at a discrete set of shift values $l_{z_j} = j\, L_z/N$, $j \in \{0, 1, \dots, N-1\}$, $N = 128$, from point measurements at N equispaced discrete locations $z_i = i\, L_z/N$, $i \in \{0, 1, \dots, N-1\}$ along the probe array. Autocorrelation is periodic and recovers unity value for all l_z that are integer multiples of L_z. Large positive and negative values at $l_z \in (0, L_z/2)$ unveil an underlying pattern. Fig. 8b shows the time-evolution of the autocorrelation function. Light (dark) regions correspond to high positive (negative) autocorrelation. The clear alternate layout of light and dark regions at some phases along the vortex-shedding cycle (see detail) indicate that the pattern is predominantly periodic. This is consistent with vortical structures arising from a global, rather than local, instability. Spanwise localisation of the pattern would translate into an oscillating but decaying autocorrelation function, with vortical structures gradually decorrelating from one another as the distance separating them grows larger. We use the first peak l_z^1 away from the origin as an indication of high correlation between adjacent streamwise-cross-stream vortices, such that it provides an indirect measurement of the preferred spanwise separation between contiguous vortical structures.

In order to trace signal-processing results back to physical flow structures, Fig. 9 depicts streamwise vorticity (ω_x) colour maps on a spanwise-cross-stream cross-section located in the wake at the same streamwise location as the sampling probe array ($x = 3$, indicated with a white line).

Spanwise-averaged contours of spanwise vorticity ($\langle\omega_z\rangle_z$) are also shown to relate the observation of streamwise-cross-stream vortices to the precise location along the Kármán vortex street (the white cross pinpoints the exact position of the probe array). Shown are eight snapshots at equispaced phases θ_i, $i \in 0, 1, \dots, 7$, duly marked and labelled in Fig. 9.

The probe array is well above the wake centre line, at the height of the top separation point on the cylinder surface, and a distance downstream such that three-dimensionality has fully developed in the braids connecting two consecutive opposite-sign Kármán vortices. At θ_0, the leading edge of the last Kármán vortex shed from the top side of the cylinder is still upstream from the sampling probe line, while the previous vortex has long left its location. No streamwise cross-stream vortices are detected by the probe and the ω_x imprints crossing the plane below it are related to the passage of the braid that connects consecutive Kármán vortices issued from the lower side. Nothing much has changed at θ_1 and θ_2, except that the leading edge of the top Kármán vortex is just reaching the probe location. Still, no traces of streamwise-cross-stream vortices are detectable. As the Kármán vortex core traverses the probe array across phases θ_3, ω_x contours indicate for the first time the appearance of three-dimensional yet diffuse vortical structures traversing the probe array. Slightly later, as the trailing edge of the Kármán vortex leaves the plane containing the probe and the bottom side of the top braid starts piercing it for θ_4,

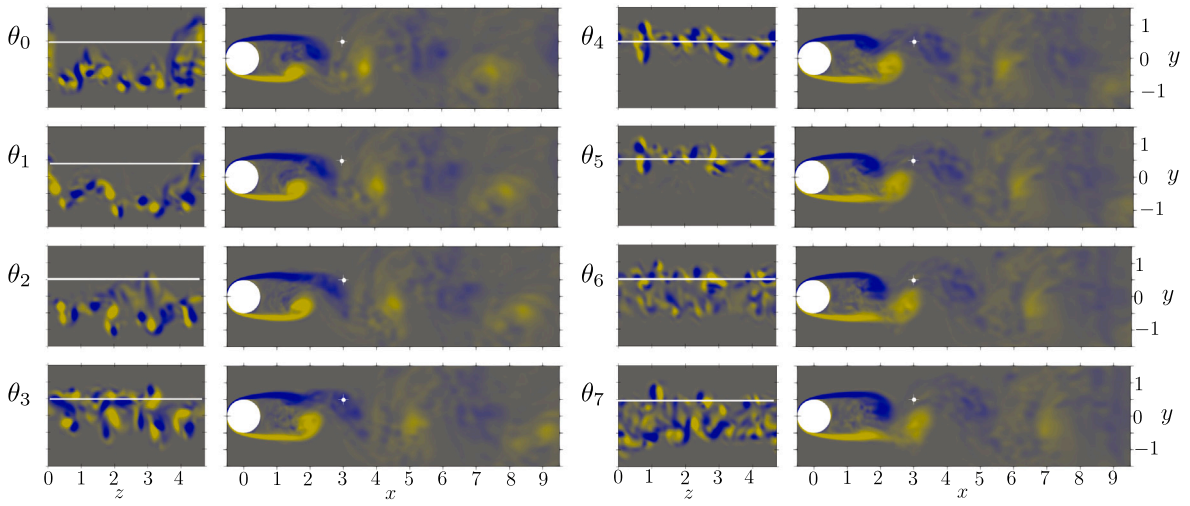

Fig. 9. Colour maps of streamwise vorticity $\omega_x \in [-5,5]$ at the $x = 3$ plane (left) and spanwise-averaged spanwise vorticity $\langle\omega_z\rangle_z \in [-5,5]$ (right) at the eight equispaced phases along the vortex-shedding cycle indicated in Fig. 8. The white solid line and bullet at $(x, y) = (3, 0.5)$ indicate the sampling probe array used for systematic signal processing.

the streamwise-cross-stream vortices become better defined and occupy a narrower band across the braid thickness that does not extend much beyond its breadth. This narrow pattern of three-dimensional vortical structures is preserved as the bulk of the braid traverses the plane for θ_5 and until at about θ_6. At θ_6 it is the upper side of the braid that is finally crossing the probe location and, although still clear, the streamwise-cross-stream vortices are accompanied by a thicker pattern that includes three-dimensionality present in the bottom Kármán vortex, which is now traversing the plane. Although not clear from the particular cycle depicted here, we will see that it is precisely at this instant that the PDF(λ_z) usually peaks in Fig. 8a, thus indicating that three-dimensionality is strongest on the external side of the braids, rather than within their thickness. Finally, at θ_7, the braid is leaving the line probe location and only some remnants of three-dimensionality are still conspicuous. Vortical patterns $\Delta\theta = \pi$ apart are statistically related by a mirror symmetry with respect to the plane $y = 0$, and although this does not hold exactly for instantaneous snapshots distant by half a period, the main characteristics of the symmetry are clearly recognisable.

For a systematic analysis of the two spanwise length scales considered, namely structure size λ_z and structure spacing l_z^1, phase averaging has been performed over the whole computational run. To do so, instantaneous samples have been classified as belonging to either one of eight equally-sized phase bins $\Delta\theta_i \in [\theta_i - \pi/8, \theta_i + \pi/8]$ ($i \in \{0, 1, 2, \ldots, 7\}$). In the case of spanwise size λ_z, the instantaneous PDFs have been phase-averaged into the eight separate phase-averaged PDFs. Instantaneous spanwise spacing l_z^1 being instead a single-valued function of time, the eight phased-averaged PDFs have been generated by considering the sequence of individual time samples as independent occurrences of a normally distributed random variable. In producing the PDFs, each sample has been weighed by the valley-to-peak height difference $A_R = R_{u'u'}(l_z^1, t) - R_{u'u'}(l_z^{0.5}, t)$, with $l_z^{0.5}$ denoting the first valley preceding the first peak in the autocorrelation function. Weighing in this way promotes the relevance of highly correlated patterns in identifying the spanwise spacing of streaks.

Fig. 10a shows the phase-averaged probability density function PDF(λ_z) of spanwise size of three-dimensional vortical structures. The PDF grows and drops along the cycle on account of the presence or absence, at the sampling location, of passing vortical structures during each particular phase, but their typical size persists at around $\lambda_z \simeq 0.33 \pm 0.01$ all along. The spanwise size of streamwise vortical structures, as measured at the same location using the same methodology, was estimated at 0.234 (ranging from 0.204 to 0.280 at different phases along the vortex shedding cycle) at the slightly higher $Re = 2000$ [22], thus evincing a declining trend of λ_z with Re. This seems to contradict Gsell et al. [7], who obtained a larger value around 0.58 at $Re = 3900$. Although the same method was used at the same streamwise-cross-stream location, the signal picked for the Hilbert transform was the fluctuation component of the actual cross-stream vorticity ω_y' and the typical size of vortical structures assessed from conditional averaging over just four vortex-shedding cycles of only the 10% most frequent local wavelengths.

Analysing instead the phase-averaged probability density function PDF(l_z^1) for the various phase bins considered (Fig. 10b) alongside the overall weighed time average (solid black line), yields conspicuously higher length scale values. The PDF peak is less stable along the full cycle and the probability peak oscillates to some degree around $l_z^1 \simeq 0.51$ for the different phases. The mean spanwise spacing is in very good agreement with the value predicted for $Re = 1500$ by the empirical scaling law of Mansy et al. [20].

The discrepancy between l_z^1 and λ_z at this value of $Re = 1500$, for which the three-dimensional pattern retains a considerable degree of spanwise periodicity, may be ascribed to nonlinearity. The vortical structures would then arise from a global, pattern-forming instability of wavelength l_z^1, but the individual nonlinear vortices have already developed a propensity to concentrate in a spanwise extent $\lambda_z < l_z^1$. This inclination becomes all the more dominant at higher flow regimes, as illustrated by Sarwar and Mellibovsky [22] at $Re = 2000$.

Lehmkuhl et al. [34] reported a very low frequency fluctuation of the vortex-formation region past a cylinder at $Re = 3900$ between what they called the low and high energy modes, each with distinct near-wake flow statistics and ensuing characteristic aerodynamic performance indicators. Although our time integration horizon is not long enough for this low frequency to show indistinctly in the power spectrum of aerodynamic force coefficients or point probe signals, Fig. 11a shows what might be interpreted as traces of such fluctuation in the drag coefficient signal C_D at $Re = 1500$. A slow oscillation about a mean value is readily observed from the smoothing of the instantaneous time series (black line) by a running average using a window of five vortex-shedding cycles (red). The amplitude of the C_D fluctuation is consistent with that reported by Lehmkuhl et al. [34], but the frequency would appear to be somewhat higher, perhaps on account of the different Re studied. We have recomputed the PDFs of Fig. 10 but applying this time conditional averaging subject to whether C_D is above or below its mean long-term value (horizontal dashed line) in order to assess the dependence of the two spanwise length scales studied on the low or high energy state of the wake. It turns out that the distributions are essentially independent, within statistical accuracy, of the wake mode

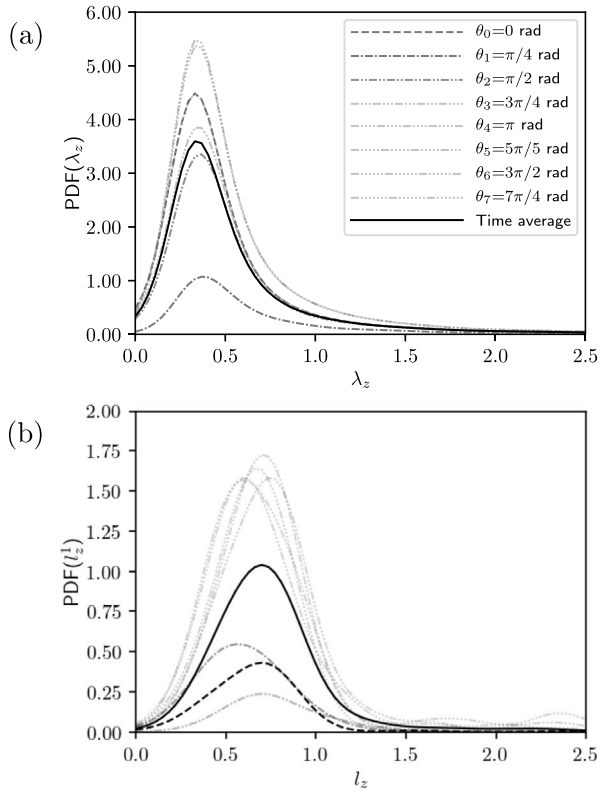

Fig. 10. Weighed time-averaged (solid line) and phase-averaged (see legend) probability density distributions of (a) spanwise size λ_z and (b) spanwise spacing l_z^1 of three-dimensional vortical structures traversing the probe array. Phase averaging is done at phases $\theta_i = i * \pi/4$ using bins $\Delta\theta_i \in [\theta_i - \pi/8, \theta_i + \pi/8]$ ($i \in \{0, 1, 2, \ldots, 7\}$). The areas below each one of the curves corresponds to the mean value of the weighing factor, *i.e.* A_ω and A_R for λ_z and l_z^1, respectively.

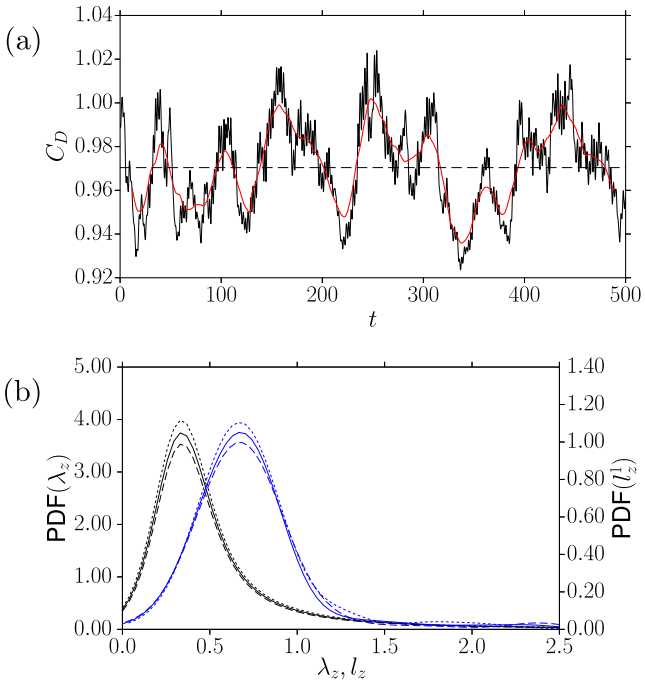

Fig. 11. (a) Low frequency fluctuation of the instantaneous drag coefficient (C_D) signal (black line), as shown by a running average (red) with window of five vertex-shedding cycles. The horizontal black dashed line indicates the signal average. (b) Weighed time-averaged probability density distributions of spanwise size λ_z (black) and spanwise spacing l_z^1 (blue) for the full (solid), and high (dashed) and low (dotted) drag states.

considered. This is clear from the conditional PDFs of λ_z and l_z^1 depicted in Fig. 11b. Only time averages are shown, but their phase-averaged counterparts reflect essentially the same independence of both length scales on the prevailing wake state. The peaks are slightly, although not significantly, higher for the low-drag state as compared to the high-drag state, but their precise location is indistinguishable. If anything, the somewhat different areas enclosed below the curves would indicate that streamwise vortices are marginally stronger and better defined, at the location tested, for the low-drag mode.

The two length scales considered have so far been measured at a unique streamwise-cross-stream location, namely $(x, y) = (3, 0.5)$. In order to gauge how l_z^1 and λ_z measurements depend on the location of the probe array, Fig. 12 depicts the evolution of both spanwise length scales along the wake at off-centreline cross-stream locations $y = 0.5$ and $y = 1.0$ together with published experimental [20] and numerical [7] results. Vortex spacing l_z^1 (blue circles and dashed line) is barely mensurable at $y = 1.0$ for $x < 5$, as the wake hardly affects this flow location (see Fig. 9), but follows thereafter a trend barely distinguishable from that observed at $y = 0.5$ (blue circles and solid line). At this cross-stream distance, the spacing of vortices slightly decreases, on average, up to $x \simeq 2$ and then initiates a gradual increase that saturates at $l_z^1 \simeq 0.75$ beyond about $x \gtrsim 10$. The spacing that might be measured at any particular time, however, is subject to wild fluctuations, as indicated by the spread of the PDF at half the peak height (error-bars). The asymptotically increasing trend we observe for l_z^1 and the match between sweeps at $y = 0.5$ and 1 is consistent with experimental observations at $Re = 600$ [20] (squares), but the curves are offset to lower values in our case. Vortex size λ_z (red circles and dashed line) is again hardly significant at $y = 1$ for $x < 3$, while clearly matching, on average, the typical vortex size at $y = 0.5$ for $x \geq 3$ (red circles and solid line). The typical size of vortex pairs, which starts close to the cylinder with $\lambda_z \simeq 0.35$ is fairly constant along the wake, with a slight increasing trend that may be related to viscous diffusion and stabilises at about 0.44 in the mid to far wake. Numerical results for λ_z at $Re = 3900$ [7] (diamonds) show somewhat larger vortex sizes. The discrepancy might be ascribed to a different definition of vortex size. Overall trends, however, are similar to those found here, particularly so in the aft portion of the wake formation region and beyond.

A third and last way of exploiting the $\tilde{\omega}_y$ signal systematically to provide a spanwise characterisation of the wake is afforded by its use in counting the number of vortices that are distinctly identifiable at each given instant. A cutoff threshold $|\tilde{\omega}_y| > 3$ has been defined to detect individual passing vortices at any given time and the vortex count established as the number of occasions in which the threshold is exceeded continuously for a spanwise extent of at least 0.1. The number of vortex pairs N_{vp} is then taken as half the number of single vortices detected. The frequency of vortex-pair count occurrences is plotted as a normalised histogram in Fig. 13. Instantaneous samples have been weighed by their degree of three-dimensionality as measured by the autocorrelation function for zero spanwise shift $R_{u'u'}(0, t)$. The height of each column thus indicates the weighed fraction of the time that N_{vp} vortex pairs are observed along the $L_z = 1.5\pi$ spanwise extent of the probe array at $(x, y) = (3, 0.5)$. The most frequent vortex-pair count is clearly $N_{vp} = 7$, which is observed for about 18% of the time. In a domain of spanwise size $L_z = 1.5\pi$, a spanwise spacing $l_z^1 = 0.70$, as obtained by signal autocorrelation, yields a typical number of vortex pairs $N'_{vp} = L_z/l_z = 6.7$, in fairly good agreement with the value obtained via direct counting of vortical structures. The sharp decay of the tail for large N_{vp} gauges the minimum wavelength into which the periodic pattern may be naturally squeezed and still persist as an eligible instability. At the other end, the substantial decrease in the frequency of occurrence of low N_{vp} constitutes a good indicator that the periodic extent of the domain is acceptable. A peak at too low N_{vp},

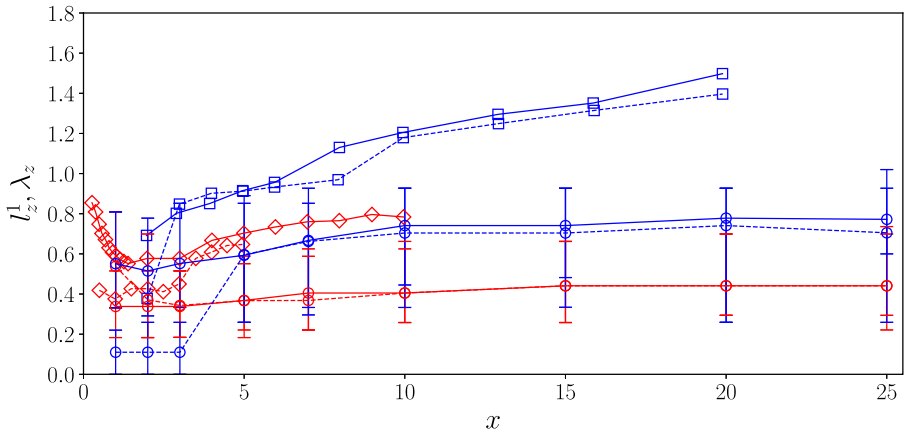

Fig. 12. Typical spanwise spacing (l_z^1, blue) and spanwise size (λ_z, red) of streamwise vortical structures at off-centerline cross-stream locations $y = 0.5$ (solid) and $y = 1.0$ (dashed) along the wake. Shown are our numerical results (circles, with error bars denoting the range for which the probability remains above half the peak probability) along with numerical results by Gsell et al. [7] at $Re = 3900$ (diamonds) and experimental results by Mansy et al. [20] at $Re = 600$ (squares).

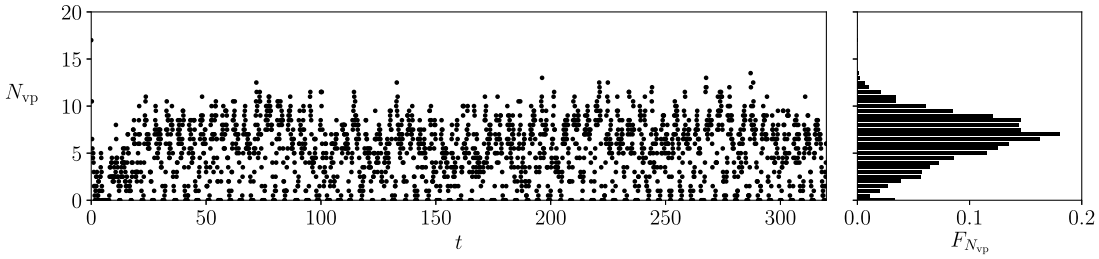

Fig. 13. Normalised and weighed frequency of observation of N_{vp} vortex pairs along the $L_z = 1.5\pi$ spanwise probe array at $(x, y) = (3, 0.5)$. The threshold for individual vortex detection is $|\tilde{\omega}_y| \geq 3$. Samples are weighed by the degree of three-dimensionality as given by $R_{u'u'}(0, t)$.

as was observed by Sarwar and Mellibovsky [22] with a domain $L_z = 2$ at $Re = 2000$, would have denoted insufficient (or barely sufficient) computational spanwise domain size, as the admissible periodic patterns would have been constrained to a very small subset of discrete wavelengths, not properly covering the actual spectrum of unstable three-dimensional modes. A certain frequency of observation of low N_{vp} naturally remains following partial vortex counts that arise whenever the streamwise-cross-stream vortices, which are mainly located along the braids connecting consecutive Kármán vortices, approach or depart from the location where the sampling probe array is located. At these particular periods, the streamwise and cross-stream inhomogeneities in the spanwise distribution of vortical structures introduces and removes these latter into and from the measurement location in succession over a short period of time rather than simultaneously and instantly.

5. Conclusions

The transitional flow past a circular cylinder at $Re = 1500$ has been comprehensively investigated. The spanwise periodic size of the computational domain has been taken sufficiently large at $L_z = 1.5\pi$ to minimise finite-domain effects, and the spanwise length scale of three-dimensional vortical flow structures arising in the wake analysed statistically.

A local approach, based on the Hilbert transform of velocity readings along a spanwise probe array, measures a typical spanwise length scale $\lambda_z \simeq 0.33$ that we relate to flow structures size. The overall three-dimensionality appears and disappears from the probe location as Kármán vortices and trailing braids cross the plane containing the probe array, but the cross-stream-streamwise vortical structures preserve about the same spanwise size all along the vortex-shedding cycle. Vortices are seen to be strongest along the outer side of the braids connecting consecutive Kármán vortices.

A second length scale is provided by a global approach based on the spanwise autocorrelation of streamwise streaks measured along the same probe array. The first autocorrelation peak is distributed around $l_z^1 \simeq 0.70$ and measures instead the typical spanwise spacing of three-dimensional vortices. The discrepancy between the two length scales can be ascribed to their measuring different aspects of three-dimensionality. They are expected to coincide at the inception of three-dimensional flow in a spanwise-invariance bifurcation on account of the spanwise dependence being modal (no harmonics in the linear regime) and the local wavelength therefore constant, independent of the location along the span and equal to the instability wavelength. As the Reynolds number is increased beyond the instability, non-linearity tends to concentrate the vortices into a smaller radius while preserving their typical spacing. Vortex pairs have been counted systematically and their number found to distribute around about $N_{vp} = 7$. This typical vortex-pair count is in fair agreement with the typical spacing measured through autocorrelation, as $l_z^1 \simeq L_z/N_{vp}$.

The results presented here at $Re = 1500$ may be compared with those reported in Sarwar and Mellibovsky [22] at $Re = 2000$, both using the same statistical estimators, to roughly assess the Reynolds number dependence of the two length scales. Comparison seems to point at a decline of streamwise vortex size λ_z, and an increase of their typical spacing, but the uncertainty in the estimation of this latter at $Re = 2000$, mainly due to insufficient spanwise extent of the domain, makes it very difficult to draw conclusions. An extensive analysis at varying Reynolds number across the transitional regime will be required to clarify how the two length scales evolve.

Finally, it might be worth exploring in the future how the length scales of streamwise vortical structures compare in wakes past bluff bodies other than circular cylinders or in the presence of upstream shear or both [41,42], for which the first three-dimensionalising instability is not the usual mode A.

CRediT authorship contribution statement

Wasim Sarwar: Design of the numerical experiments, Numerical simulations, Post-processing of results, Analysis of results, Writing – original draft. **Reda El Mansy:** Post-processing of results, Analysis of results, Writing – original draft. **Josep M. Bergadà:** Project supervision, Analysis of results, Writing – original draft. **Fernando Mellibovsky:** Project supervision, Design of the numerical experiments, Analysis of results, Writing – original draft.

Declaration of competing interest

The authors declare that they have no known competing financial interests or personal relationships that could have appeared to influence the work reported in this paper.

Data availability

Data will be made available on request.

Acknowledgements

This work has been financed by the Spanish and Catalan Governments under grants FIS2016-77849-R/PID2020-114043GB-I00 and 2017-SGR-00785, respectively. The authors also thankfully acknowledge the computer resources at MareNostrum and Calendula accessed through grants RES-FI-2017-2-0020 and RES-FI-2017-3-0009, respectively. F. Mellibovsky is a Serra-Húnter fellow.

References

[1] Williamson CHK, Govardhan R. Vortex-induced vibrations. Annu Rev Fluid Mech 2004;36(1):413–55.
[2] Mahir N, Altaç Z. Numerical investigation of convective heat transfer in unsteady flow past two cylinders in tandem arrangements. Int J Heat Fluid Flow 2008;29(5):1309–18.
[3] Choi H, Jeon WP, Kim J. Control of flow over a bluff body. Annu Rev Fluid Mech 2008;40:113–39.
[4] Dong S, Karniadakis GE, Ekmekci A, Rockwell D. A combined direct numerical simulation–particle image velocimetry study of the turbulent near wake. J Fluid Mech 2006;569:185–207.
[5] Konstantinidis E, Balabani S. Flow structure in the locked-on wake of a circular cylinder in pulsating flow: Effect of forcing amplitude. Int J Heat Fluid Flow 2008;29(6):1567–76.
[6] Norberg C. LDV-measurements in the near wake of a circular cylinder. ASME paper no. FEDSM98-521, 1998.
[7] Gsell S, Bourguet R, Braza M. Three-dimensional flow past a fixed or freely vibrating cylinder in the early turbulent regime. Phys Rev Fluids 2018;3:013902.
[8] Ma X, Karamanos GS, Karniadakis GE. Dynamics and low-dimensionality of a turbulent near wake. J Fluid Mech 2000;410:29–65.
[9] Howe MS. Frontmatter. In: Acoustics of fluid-structure interactions. Cambridge monographs on mechanics, Cambridge University Press; 1998, p. i–vi.
[10] Sarwar W. Active flow control methods for aerodynamic applications (Ph.D. thesis), Universitat Politècnica de Catalunya; 2020.
[11] Sarwar W, Bergadà JM, Mellibovsky F. Onset of temporal dynamics within a low Reynolds-number laminar fluidic oscillator. Appl Math Model 2021;95:219–35.
[12] Williamson CHK. The existence of two stages in the transition to three-dimensionality of a cylinder wake. Phys Fluids 1988;31(11):3165–8.
[13] Roshko A. On the development of turbulent wakes from vortex streets. Technical report 1191, National Advisory Committee for Aeronautics; 1954.
[14] Bloor MS. The transition to turbulence in the wake of a circular cylinder. J Fluid Mech 1964;19(2):290–304.
[15] Gerrard JH. Experimental investigation of seperated boundary layer undergoing transition to turbulence. Phys Fluids 1967;10(9P2):S98–&.
[16] Unal MF, Rockwell D. On vortex formation from a cylinder. Part 1. The initial instability. J Fluid Mech 1988;190:491–512.
[17] Prasad A, Williamson CHK. The instability of the shear layer separating from a bluff body. J Fluid Mech 1997;333:375–402.
[18] Kourta A, Boisson HC, Chassaing P, Minh HH. Nonlinear interaction and the transition to turbulence in the wake of a circular cylinder. J Fluid Mech 1987;181:141–61.
[19] Norberg C. Effects of Reynolds number and a low-intensity freestream turbulence on the flow around a circular cylinder. Technical report 87/2, Göteborg, Sweden: Chalmers University; 1987.
[20] Mansy H, Yang PM, Williams DR. Quantitative measurements of three-dimensional structures in the wake of a circular cylinder. J Fluid Mech 1994;270:277–96.
[21] Camussi R. Coherent structure identification from wavelet analysis of particle image velocimetry data. Exp Fluids 2002;32(1):76–86.
[22] Sarwar W, Mellibovsky F. Characterization of three-dimensional vortical structures in the wake past a circular cylinder in the transitional regime. Phys Fluids 2020;32(7):074104.
[23] Chyu CK, Rockwell D. Near-wake structure of an oscillating cylinder: effect of controlled shear-layer vortices. J Fluid Mech 1996;322:21–49.
[24] Chen G, Xiong Q, Morris PJ, Paterson Eric G, Sergeev A, Wang Y. OpenFOAM for computational fluid dynamics. Notices Amer Math Soc 2014;61(4):354–63.
[25] Ferziger Joel H, Perić Milovan, Street Robert L. Computational methods for fluid dynamics, Vol. 3. Springer; 2002.
[26] Chen H, Li Z, Zhang Y. U or V shape: Dissipation effects on cylinder flow implicit large-eddy simulation. AIAA J 2016;55(2):459–73.
[27] Lodato G, Jameson A. LES modeling with high-order flux reconstruction and spectral difference schemes. In: ICCFD7 conference 2012, Vol. 2201. 2012, p. 9–13.
[28] Mohammad AH, Wang ZJ, Liang C. Large eddy simulation of flow over a cylinder using high-order spectral difference method. Adv Appl Math Mech 2010;2(4):451–66.
[29] Wissink JG, Rodi W. Numerical study of the near wake of a circular cylinder. Int J Heat Fluid Flow 2008;29(4):1060–70.
[30] Ramberg S, Griffin Owen M. The effects of vortex coherence, spacing, and circulation on the flow-induced forces on vibrating cables and bluff structures. Report, Naval Research Lab.; 1976.
[31] Evangelinos C. Parallel simulations of vortex-induced vibrations in turbulent flow: linear and nonlinear models. Brown University; 1999.
[32] Norberg C. Fluctuating lift on a circular cylinder: review and new measurements. J Fluids Struct 2003;17(1):57–96.
[33] Konstantinidis E, Balabani S, Yianneskis M. The effect of flow perturbations on the near wake characteristics of a circular cylinder. J Fluids Struct 2003;18(3–4):367–86.
[34] Lehmkuhl O, Rodríguez I, Borrell R, Oliva A. Low-frequency unsteadiness in the vortex formation region of a circular cylinder. Phys Fluids 2013;25(8):085109.
[35] Norberg C. An experimental investigation of the flow around a circular cylinder: influence of aspect ratio. J Fluid Mech 1994;258:287–316.
[36] Ong L, Wallace J. The velocity field of the turbulent very near wake of a circular cylinder. Exp Fluids 1996;20(6):441–53.
[37] Parnaudeau P, Carlier J, Heitz D, Lamballais E. Experimental and numerical studies of the flow over a circular cylinder at Reynolds number 3900. Phys Fluids 2008;20(8):085101.
[38] Lin J-C, Towfighi J, Rockwell D. Instantaneous structure of the near-wake of a circular cylinder: on the effect of Reynolds number. J Fluids Struct 1995;9(4):409–18.
[39] Williamson CHK. Vortex dynamics in the cylinder wake. Annu Rev Fluid Mech 1996;28:477–539.
[40] Williamson CHK. Three-dimensional wake transition. J Fluid Mech 1996;328:345–407.
[41] El Mansy R, Sarwar W, Bergadà JM, Mellibovsky F. Square cylinder in the interface of two different velocity streams. J Fluid Mech 2022;950:A30.
[42] El Mansy R, Bergadà JM, Sarwar W, Mellibovsky F. Aerodynamic performances and wake topology past a square cylinder in the interface of two different-velocity streams. Phys Fluids 2022;34(6):064106.